

DOI: 10.1002/elan.202060058

Template-free Electrosynthesis of Platinum Nano-Cauliflowers for Catalysing Electron Transfer Reaction of Plutonium

Arvind S. Ambollikar^[a, b] and Saurav K. Guin^{*[a]}

Abstract: A coupled-oxido-reductive multiple-potentiostatic pulse strategy was developed to electrochemically prepare platinum-nano-cauliflowers (PtNCFs) on indium-tin-oxide (ITO) coated glass electrode. The mechanism of electrocrystallization was studied during the formation of

PtNCFs on ITO. By virtue of that synthesis strategy, the PtNCFs/ITO surface could catalyse the quasi-reversible electron transfer reaction of plutonium (Pu) (IV)/(III) redox couple in aqueous sulphuric acid solution compared to bare ITO.

Keywords: Electrocatalysis · Electrocrystallization · Platinum nano-cauliflowers · Heterogeneous electron transfer rate constant · Plutonium

1 Introduction

Metal nanoparticles are the present and future of catalysis by virtue of large surface-area-to-volume ratio, large surface energies, specific electronic structure, short range ordering, and high number of kinks and low-coordination sites such as corners, edges and dangling bonds [1–4]. Electrosynthesis is a room-temperature solution phase route to prepare supported metal nanoparticles on electrodes by transferring electrons from external source to the metal ion precursor present in the solution. Although this process can produce metal nanoparticles of best possible chemical purity, the control of size and shape of nanoparticles is very challenging task as it depends on several parameters such as strategy of electrochemical synthesis [5,6], potential pulse parameters [7], nature of the substrate materials [8], and presence of any additional chemical reagents [9]. Different strategies had been adapted to date to prepare platinum nanoparticles of different sizes and shapes by employing cyclic voltammetry at constant scan rate [10] and potentiostatic pulses [11–13]. Further, it has been observed that the interfacial strain on the platinum nanoparticles supported on an oxide matrix can enhance its catalytic activity [14,15].

Plutonium (Pu) is one of the important artificial elements useful for atomic energy, which is an established non-conventional source of energy. Therefore, accurate and precise determination of Pu in metal oxide/carbide fuels is a desirable job to assure the performance of nuclear fuels inside nuclear reactors and electrochemistry (such as coulometry, biamperometry, etc in sulphuric acid solutions) is trying to serve this purpose [16–18]. The heterogeneous electron transfer reaction of Pu(IV)/Pu(III) is found to be an electrochemically quasi-reversible redox reaction, which greatly depends on the nature of the electrode materials. Hence, the electrochemistry of Pu(IV)/Pu(III) had been investigated on glassy carbon

electrode [19], platinum electrode [20], and electrodes modified with platinum nanoparticles [10], ruthenium nanoparticles [21], poly(3,4-ethylenedioxythiophene) polystyrene sulfonate [22,23], polyaniline and single-walled carbon nanotubes [24], graphene [25], and electrochemically reduced graphene oxide [26]. However, none of the modified electrodes practically could be able to replace the conventional Pt electrode for the routine electrochemical analysis of Pu. Hence, our interest was to improve the performance of Pt electrode itself by modifying its structure, enhancing electrochemically active surface area and number of active sites. In this direction, this paper demonstrates the formation of a coupled-oxido-reductive multiple-potentiostatic pulse strategy to prepare platinum-nano-cauliflowers (PtNCFs) on indium-tin-oxide (ITO) coated glass electrode. The process of electrocrystallization was investigated during the formation of PtNCFs and its morphology and crystal structures were characterized after the synthesis. The electrochemical electron transfer reaction of Pu(IV)/Pu

[a] A. S. Ambollikar, Dr. S. K. Guin
Fuel Chemistry Division, Bhabha Atomic Research Centre,
Trombay, Mumbai-400085, India
Tel.: +91-22-2559-4591
Fax: +91-22-2550-5151
E-mail: sauravkrquin@yahoo.co.in
skguin@barc.gov.in

[b] A. S. Ambollikar
Homi Bhabha National Institute, Anushakti Nagar, Mumbai –
400094, India.

 Supporting information for this article is available on the WWW under <https://doi.org/10.1002/elan.202060058>
This manuscript is part of a special issue *EIHE-2020: Spectrum of Electroanalysis in India* published through standard peer-review process from the selected presentations made in EIHE-2020, Mumbai, India during Jan 21–25, 2020.

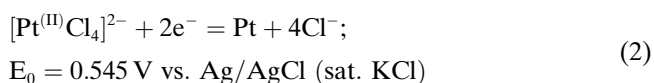
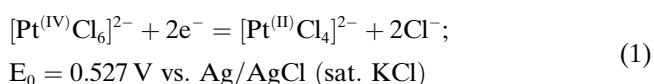
(III) in sulphuric acid (H_2SO_4) on PtNCFs/ITO was studied in comparison to ITO electrode.

2 Experimental

Hexachloroplatinic acid (H_2PtCl_6), hydrochloric acid (HCl), potassium ferricyanide ($\text{K}_3[\text{Fe}(\text{CN})_6]$), H_2SO_4 of AR grades were used in the studies without any pre-treatment. A stock solution of known concentration of Pu was prepared from anhydrous potassium plutonium sulphate dihydrate ($\text{K}_4\text{Pu}(\text{SO}_4)_4$) following our optimized method as described in details elsewhere [26]. Authors declare a precautionary statement to readers about handling Pu that it is a radioactive material and thus must be used in safe radiological facilities with proper training. Ultrapure Milli-Q Millipore water and high-purity argon gas were used to prepare all the solutions and purging out dissolved oxygen from solutions, respectively. The ITO electrode (sheet resistance 8–12 Ω/sq) was cleaned with acetone and sonicated in Millipore water for 10 minutes followed by drying with an argon gas stream. The clean ITO electrodes were covered from four sides by clean parafilm to expose about 1 cm^2 geometrical area for electrochemistry. The electrochemical experiments were performed at lab temperature ($25 \pm 1^\circ\text{C}$) with Autolab PGSTAT30 and CHI 450B electrochemical workstations. The spiral platinum wire and Ag/AgCl (satd. KCl) were used as the counter and reference electrodes, respectively. The Rigaku Smart Lab X-ray diffractometer with a Cu-K α excitation source and Carlzeiss Auriga Crossbeam Field emission-scanning electron microscope (FE-SEM) were used for the x-ray diffraction (XRD) and surface morphological analysis of the modified electrode, respectively. The detailed parameters for each experiment are stated before discussing the respective result and in the caption of the corresponding figure in the next section so that anyone can reproduce the observation.

3 Results and Discussion

The desired shape and structure of PtNCFs insisted us to develop a template-free electrochemical strategy for successive multiple nucleation and growth of Pt preferably over Pt-nuclei already deposited on ITO electrode. In general, the reduction of $[\text{Pt}^{(\text{IV})}\text{Cl}_6]^{2-}$ to Pt happens in solution in two steps of different standard reduction potentials (E_0 s) (Eq. 1,2) [27]:



However, the heterogeneous reduction of $\text{H}_2[\text{Pt}^{(\text{IV})}\text{Cl}_6]$ to Pt is different and especially in the presence of acids

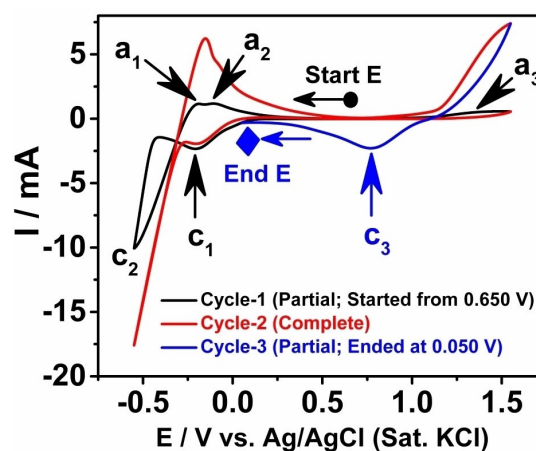


Fig. 1. CV of 10 mM H_2PtCl_6 in 1 M HCl on ITO electrode. $\nu = 50 \text{ mV s}^{-1}$.

because HCl is produced as the reaction product after the deposition process [11–13]. Thus, the cyclic voltammogram (CV) of 10 mM H_2PtCl_6 in 1 M HCl on ITO was studied carefully for a few initial cycles at the scan rate (ν) of 50 mV s^{-1} to get an insight into the electrochemical phase-formation of Pt on ITO (Figure 1).

During the potential scan starting from 0.650 V towards the lower potentials (black line, Cycle-1), the reduction of $[\text{Pt}^{(\text{IV})}\text{Cl}_6]^{2-}$ to Pt on ITO was observed at very high kinetic overpotential with a cathodic peak at -0.208 V (c_1). This phenomenon is in concord with earlier observations of Pt deposition on various substrates at different acids [28–30]. The reduction of H^+ to H-atom (H_{ad}) on Pt-nuclei started at potentials $\leq -0.408 \text{ V}$ and it continued in parallel to the Pt deposition until the scan-reversal potential (-0.550 V). Up to that point, the ITO surface was expected to be populated with Pt-nuclei and thus during the reverse potential scan towards higher potentials than -0.550 V (black line, Cycle-1) the reduction of H^+ continued at much lesser cathodic overpotentials leading to a current-crossover at -0.314 V . The small anodic humps at -0.189 V (a_1) and -0.152 V (a_2) are attributed to the desorption of H_{ad} from {110} and {100} crystal planes of Pt-nuclei [31]. At further positive potential the observed anodic peak (a_3) at 1.102 V represented oxidative leaching of deposited Pt on ITO to the complex forming electrolyte (i.e., HCl) as well as partial surface oxidation of Pt to surface oxides of Pt [32–37]. The current of all representative peaks increased in Cycle-2 (red line). Although, the reduction of $[\text{Pt}^{(\text{IV})}\text{Cl}_6]^{2-}$ happened at similar potential (-0.205 V), the H^+ reduction started at much lesser negative potential (i.e. at -0.265 V) and both desorption peaks of H_{ad} were amplified and merged with each other leading to a single peak at -0.108 V (Cycle-2; red line). Further, the extents of leaching and surface oxidation of Pt-nuclei on ITO were also increased in Cycle-2 (red line) as indicated from the higher current of a_3 and appearance of an additional

cathodic peak (c_3) at 0.768 V representing significant reduction of surface oxides in *Cycle-3* (blue line).

The above mentioned observations were the key incentives to design and optimize a multiple-potentiostatic-pulse-strategy for the template-free electrochemical synthesis of PtNCFs on ITO as schematically shown in Figure 2. Our strategy involved *three* basic components (as summarized in Table S1 in the *Supporting Information File*): (i) *Precondition*: The electrode-electrolyte interface plays a crucial role in the nucleation and growth phenomenon [5,7,8]. Thus, the ITO electrode was initially kept at a precondition potential ($E_p=0.35$ V; where Pt deposition did not set-in) for 10 s to establish a stable electrode-electrolyte interface at ITO immersed in a solution of 10 mM H_2PtCl_6 in 1 M HCl. (ii) *Single cycle of nucleation-oxidation-oxide reduction*: A nucleation pulse (N) of high cathodic overpotential ($E_N=-0.55$ V) for very short duration (0.2 s) was implemented to seed sufficient number of Pt-nuclei on ITO in controlled manner, followed by the application of a short (of duration 0.2 s) oxidation pulse (O) at high anodic potential ($E_O=1.55$ V) for oxidative leaching of sub-critical Pt-nuclei and partial surface oxidation of Pt-nuclei. Then, the surface oxides of residual Pt-nuclei were reduced by applying an oxide-reduction pulse (OR) at 0.65 V (E_{OR}) for sufficient longer duration (i.e. 0.6 s) to instantly generate active site on residual Pt-nuclei for inducing fresh nucleation in the next cycle. This sequence of pulses was applied for only one cycle to avoid any fresh nucleation on the electrode surface except the residual Pt-nuclei in the next cycles. (iii) *1000 cycles of growth-oxidation-oxide reduction*: The freshly reduced surface

oxides (formed during the oxide-reduction step) situated on the residual Pt-nuclei deposited on ITO can act themselves as active sites during the reduction of $[Pt^{(IV)}Cl_6]^{2-}$ in the consecutive cycles. Thus the growth pulses (G_n , $n=1-1000$) of lower overpotential ($E_G=-0.50$ V) for 0.2 s were applied to form seeds of Pt over residual regenerated Pt-nuclei remained at the end of previous cycle. To avoid uncontrolled leaching of Pt during the oxidation pulses (O_n , $n=1-1000$), lower oxidation potential (at 1.30 V) compared to that of the first cycle was used keeping the parameters of the OR pulses (OR_n , $n=1-1000$) unaltered for 1000 cycles (n).

The optimized pulse sequence and parameters are shown in Figure 3[A]. Figure 3[B] shows the corresponding chronoamperogram for the formation of PtNCFs during the application of the pulse sequence shown in Figure 3[A]. The progressive increase in the growth, oxidation and oxide-reduction currents in the consecutive cycles represented progressive formation of PtNCFs on ITO. A careful observation revealed that, along with the progress of that electrodeposition process through multiple-potentiostatic-pulse-chain, the base current and start-time of each component of chronoamperometric current transient were found to be different compared to its earlier values. Thus for comparative analysis of the individual chronoamperograms, we subtracted the actual base-current value (i.e. current just prior to the application of the potential pulse of interest) and actual start-time value (i.e. just prior to the application of the potential pulse of interest) of the current transient of interest from the current and time data. The normalized current and time for each transient are denoted as I_{Norm}

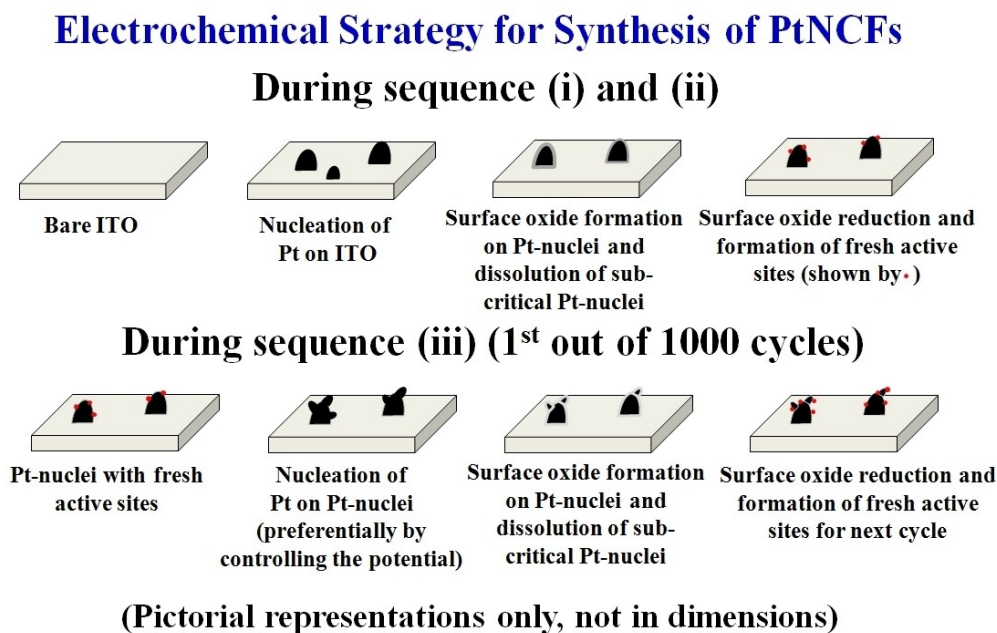


Fig. 2. The schematic representation of the multiple-potentiostatic-pulse-strategy for the template-free electrochemical synthesis of PtNCFs on ITO.

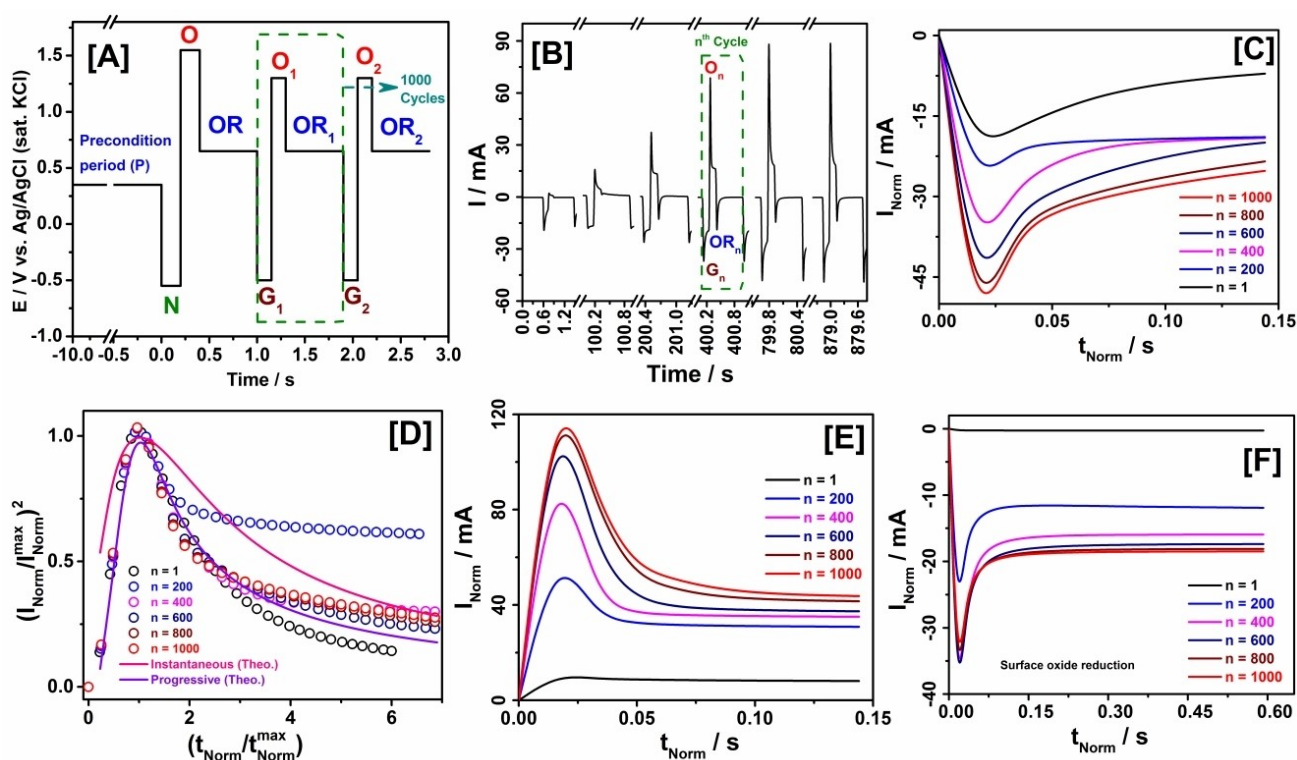


Fig. 3. **[A]** The multiple-potentiostatic-pulse-strategy for the template-free electrochemical synthesis of PtNCFs on ITO and **[B]** corresponding chronoamperogram recorded during the formation of PtNCFs. The normalized and overlaid chronoamperometric current transients corresponding to the **[C]** fresh-nucleation followed by growth pulse, **[E]** oxidation and **[F]** oxide-reduction pulses at 1st, 200th, 400th, 600th, 800th and 1000th growth cycle (*n*). **[D]** Non-dimensional plots of $[I_{\text{Norm}}/I_{\text{Norm}}^{\text{Max}}]^2$ versus $t_{\text{Norm}}/t_{\text{Norm}}^{\text{Max}}$ for each current transient shown in **[C]** in comparison to the theoretically calculated currents of instantaneous and progressive nucleation and growth phenomena as modeled by Scharifker and Hills.

and t_{Norm} , respectively. Figure 3[C] shows the normalized and overlaid chronoamperometric current transients corresponding to the fresh-nucleation followed by growth of Pt on residual activated Pt-nuclei at 1st, 200th, 400th, 600th, 800th and 1000th growth cycle (*n*). The cathodic current for each transient increased initially with time due to the electrodeposition of new Pt-nuclei on the freshly regenerated active sites of the residual Pt-nuclei left on the ITO surface at the end of previous OR pulse. The overall electroactive surface area of the Pt-deposits on ITO and hemi-spherical mass-transfer of $[\text{Pt}^{(\text{IV})}\text{Cl}_6]^{2-}$ ions around the active sites were dynamically increased during that electrodeposition process and thus it also contributed to the progressive enhancement of current with time up to a maxima ($I_{\text{Norm}}^{\text{Max}}$) at about 20–25 ms ($t_{\text{Norm}}^{\text{Max}}$). Then the diffusion zones of $[\text{Pt}^{(\text{IV})}\text{Cl}_6]^{2-}$ ions around the adjacent active sites started overlapping among themselves and progressively it created depletion zones of $[\text{Pt}^{(\text{IV})}\text{Cl}_6]^{2-}$ ions around some of the active sites. Thus the cathodic current started decreasing with time and at longer duration the hemi-spherical mass transfer of $[\text{Pt}^{(\text{IV})}\text{Cl}_6]^{2-}$ ions around each active site was suppressed by the linear mass transfer of $[\text{Pt}^{(\text{IV})}\text{Cl}_6]^{2-}$ ions from the bulk of the solution towards the working electrode. The relative enhancement of the amperometric current was more

prominent in the initial cycles compared to the later cycles and it might be attributed to the progressive depletion of local concentrations of $[\text{Pt}^{(\text{IV})}\text{Cl}_6]^{2-}$ ions around the interface of working electrode (WE) and electrolyte during the progress of the electrodeposition.

The general feature of the nucleation and growth of fresh Pt-nuclei on the rejuvenated active sites on the pre-deposited Pt was studied by comparing the non-dimensional plots of $[I_{\text{Norm}}/I_{\text{Norm}}^{\text{Max}}]^2$ versus $t_{\text{Norm}}/t_{\text{Norm}}^{\text{Max}}$ (Figure 3 [D]) of each current transient shown in Figure 3[C] in comparison to the theoretically calculated currents of instantaneous (Eq. 3) and progressive (Eq. 4) nucleation and growth phenomena as modeled by Scharifker and Hills [38].

$$(I_{\text{Norm}}/I_{\text{Norm}}^{\text{Max}})_{\text{Instantaneous}}^2 = 1.9542 \{1 - \exp[-1.2564(t_{\text{Norm}}/t_{\text{Norm}}^{\text{Max}})]\}^2 / (t_{\text{Norm}}/t_{\text{Norm}}^{\text{Max}}) \quad (3)$$

$$(I_{\text{Norm}}/I_{\text{Norm}}^{\text{Max}})_{\text{Progressive}}^2 = 1.2254 \{1 - \exp[-2.3367(t_{\text{Norm}}/t_{\text{Norm}}^{\text{Max}})^2]\}^2 / (t_{\text{Norm}}/t_{\text{Norm}}^{\text{Max}}) \quad (4)$$

It can be clearly seen that the re-nucleation followed by growth phenomenon was mostly progressive in nature.

However, we could not perform further analysis of the chronoamperometric transients as many electrochemical nucleation and growth parameters such as electrochemically active surface area, number of deposited nuclei and rate of nucleation were too much interdependent among themselves and dynamic during the progress of the studied electrodeposition process. The anodic current transient represents an overall oxidative leaching of Pt to chloroplatinate complexes and potential-induced surface oxide formation with time (Figure 3[E]). At each cycle, this process became predominant after 20–25 ms from the application of the oxidation pulse and then reached to a steady-state value. The overall anodic current was found to be negligible in the first growth cycle, whereas it significantly increased with increase in the amount of residual Pt-nuclei on ITO at higher growth cycles. The similar trend was also observed for the current transients correspond to the oxide-reduction pulse (Figure 3[F]). The long plateau at the tail of each oxide-reduction current transient could assure the accomplishment of the fresh surface regeneration. This continuous multiple-potentiostatic pulse sequence of different potentials were designed and optimized to form the cauliflower type structures of Pt on ITO and its successful production (after 1000 growth cycles) could be seen from the FE-SEM images of the PtNCFs/ITO (Figure 4[A]). The overall nanostructure was actually found to be an aggregate of small near-to-spherical Pt nanoparticles of average diameter 60–70 nm formed one on another as a result of the designed multiple-potentiostatic pulse sequence. Inset shows the magnified image of PtNCF revealing its shape and the structural morphology. The XRD pattern of PtNCFs/ITO as shown in Figure 4[B] represents the diffraction peaks correspond to (111), (200), (220), (311) and (222) group of crystal planes of metallic Pt at 2θ values of 39.8°, 46.3°, 67.6°, 81.4°, and 86.7°, respectively. The presence of multiple planes in the XRD pattern confirmed the polycrystalline nature of the

electrodeposited PtNCFs on ITO, whose representatives peaks are marked with asterisk in Figure 4[B].

The electrochemistry of 7.6 mg/mL $[\text{Pu}^{\text{IV}}(\text{SO}_4)_4 \cdot (\text{H}_2\text{O})_4]^{4-}$ [39] (i. e. 31.8 mM Pu) in 1 M H_2SO_4 was initially investigated on (a) ITO, (b) Pt and (c) PtNCFs/ITO working electrodes by [A] CV at a scan rate of 0.025 V s^{-1} and [B] Nyquist plot of electrochemical impedance spectroscopy (EIS) at 0.575 V with a sine potential perturbation of amplitude 0.01 V and linear frequency in the range 1×10^5 – 1×10^{-1} Hz (Figure 5). All the working electrodes were believed to be possessed with different electrochemically active surface areas (A_e). Thus A_e s of ITO, Pt and PtNCFs/ITO were calculated as 1.09, 0.055 and 1.33 cm^2 , respectively, from the slopes of the plots of cathodic peak current (i_p^c) versus scan rate (v , in the range 0.01– 0.05 V s^{-1} at the step of 0.01 V s^{-1}) by using the Randles-Sevcik equation (Eq. 5) for CVs of 5 mM $\text{K}_3[\text{Fe}(\text{CN})_6]$ in 0.1 M KCl on those working electrodes.

$$i_p^c = 2.69 \times 10^5 n^{3/2} C_0 D^{1/2} A_e v^{1/2} \quad (5)$$

where, n , C_0 and D are the number of electrons involved in the redox process (here $n=1$), concentration (here $C_0=5 \times 10^{-6} \text{ mol cm}^{-3}$) and diffusion coefficient (here $D=7.6 \times 10^{-6} \text{ cm}^2 \text{ s}^{-1}$) of $\text{K}_3[\text{Fe}(\text{CN})_6]$ [40], respectively. The comparative CVs as shown in Figure 5[A] were plotted with respect to the corresponding current density (j), which was calculated by dividing the experimentally recorded current with the corresponding A_e s. It can be seen that the electrochemistry (in terms of the relative shapes of the voltammograms) of $[\text{Pu}^{\text{IV}}(\text{III})\text{SO}_4)_4 \cdot (\text{H}_2\text{O})_4]^{4-}$ redox reaction was highly improved on PtNCFs/ITO compared to bare ITO. However, except the enhancement of current density values, no significant change was observed on PtNCFs/ITO compared to bare Pt. This might be attributed to the influence of shapes of PtNCFs towards the mass transfer of the analytes in their vicinity. The cathodic (E_p^c) and anodic (E_p^a) peak potentials of Pu(IV)/Pu(III) electron transfer reaction were

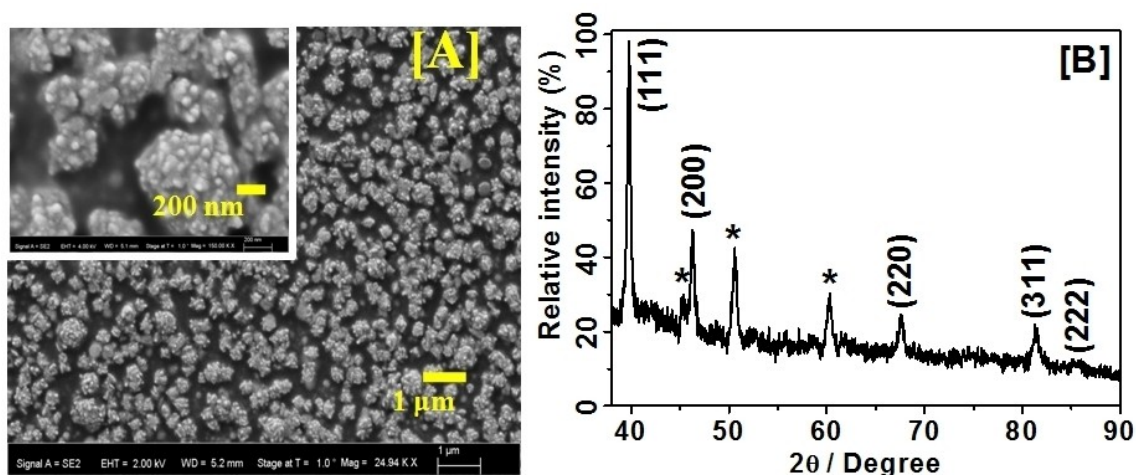


Fig. 4. [A] FE-SEM images and [B] XRD pattern of the PtNCFs/ITO. Inset: Magnified image of part of the area of [A].

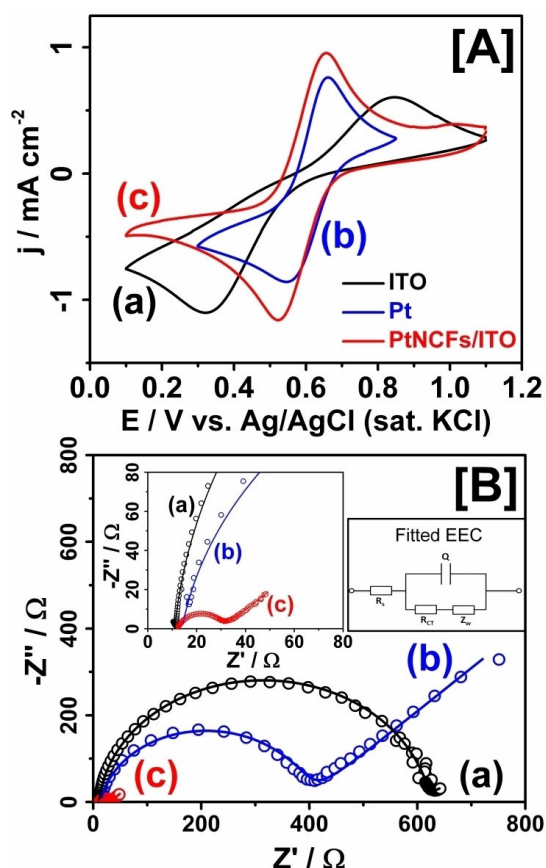


Fig. 5. [A] CV at $v=0.025 \text{ V s}^{-1}$ and [B] Nyquist plot of $7.6 \text{ mg mL}^{-1} [\text{Pu}^{\text{IV}}(\text{SO}_4)_4 \cdot (\text{H}_2\text{O})_4]^{4-}$ (i.e. 31.8 mM Pu) in $1 \text{ M H}_2\text{SO}_4$ on (a) ITO, (b) Pt and (c) PtNCFs/ITO working electrodes. For [B], fixed potential = 0.575 V , sine potential perturbation of amplitude = 0.01 V and linear frequency = $1 \times 10^2 - 1 \times 10^{-1} \text{ Hz}$. The best fitted electrochemical equivalent circuit (EEC) is shown in the right-hand side inset, while the left-hand side inset shows the magnified view of [B] in the high frequency region.

shifted from 0.320 V and 0.846 V on ITO electrode to 0.523 V and 0.657 V on PtNCFs/ITO.

As a result, the decrease in the peak-to-peak potential difference (ΔE_p) from 0.526 V on ITO to 0.134 V on PtNCFs/ITO suggested an improvement in the electrochemical reversibility of the $\text{Pu}(\text{IV})/\text{Pu}(\text{III})$ electron transfer reaction upon embedded PtNCF structures on ITO surface. The Nyquist plot (Figure 5[B]) showed a systematic decrease of the charge transfer resistance (R_{CT}) of the $\text{Pu}(\text{IV})/\text{Pu}(\text{III})$ electron transfer reaction from 603.7Ω at ITO electrode to 378.7Ω at Pt and 18.4Ω at PtNCFs/ITO electrodes (Table 1). The significant changes in the ΔE_p and R_{CT} at PtNCFs/ITO compared to ITO encouraged us to study the $\text{Pu}(\text{IV})/\text{Pu}(\text{III})$ electron transfer reaction on these two electrodes in further detail.

Figure 6 shows the CV of $7.6 \text{ mg mL}^{-1} [\text{Pu}^{\text{IV}}(\text{SO}_4)_4 \cdot (\text{H}_2\text{O})_4]^{4-}$ in $1 \text{ M H}_2\text{SO}_4$ on [A] ITO and [B] PtNCFs/ITO at $v=0.025, 0.050, 0.075, 0.100, 0.150, 0.200, 0.250$ and 0.300 V s^{-1} . The corresponding peak parameters such as j_p^c , E_p^c , E_p^a , ΔE_p and potential at half-peak

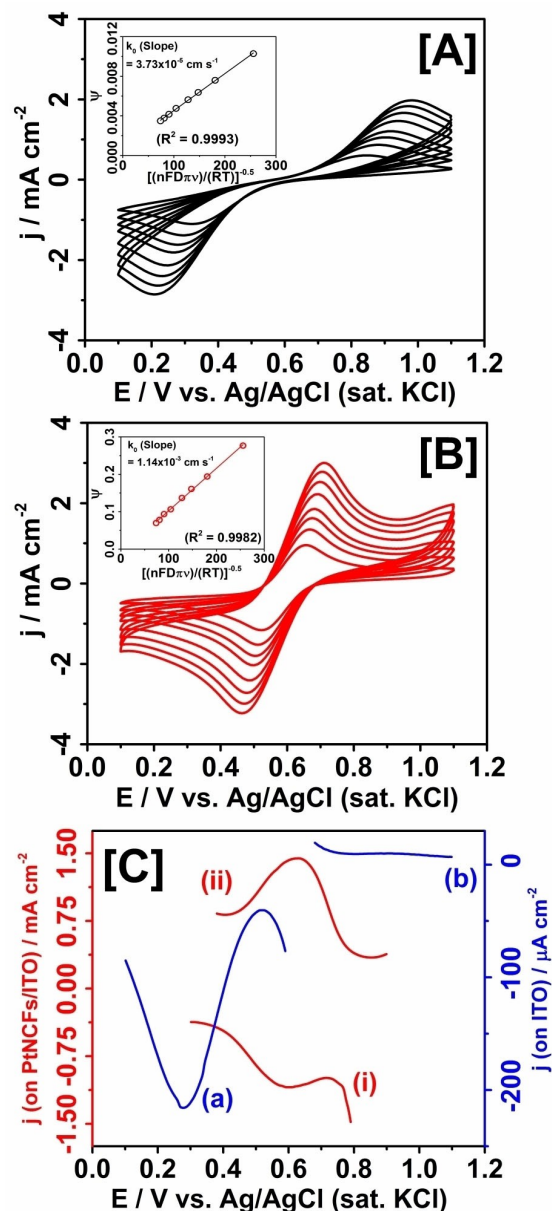


Fig. 6. CVs of $7.6 \text{ mg mL}^{-1} [\text{Pu}^{\text{IV}}(\text{SO}_4)_4 \cdot (\text{H}_2\text{O})_4]^{4-}$ in $1 \text{ M H}_2\text{SO}_4$ on [A] ITO and [B] PtNCFs/ITO at $v=0.025, 0.050, 0.075, 0.100, 0.150, 0.200, 0.250$ and 0.300 V s^{-1} . [C] Cathodic (a, i) and anodic (b, ii) square wave voltammograms (SWVs) of $7.6 \text{ mg mL}^{-1} [\text{Pu}^{\text{IV}}(\text{SO}_4)_4 \cdot (\text{H}_2\text{O})_4]^{4-}$ in $1 \text{ M H}_2\text{SO}_4$ on ITO and PtNCFs/ITO electrodes. SWV Parameters: Amplitude = 0.025 V ; Linear frequency = 20 Hz ; Step-potential increment = 0.001 V .

(cathodic) ($E_{p/2}^c$) are shown in Table 2. For both the electrodes, E_p^c and E_p^a shifted towards less-positive and more-positive potentials, respectively, with increasing the scan rates. This suggested the heterogeneous quasi-reversible electron transfer reaction of $\text{Pu}(\text{IV})$ and $\text{Pu}(\text{III})$ on both ITO and PtNCFs/ITO electrodes. The cathodic charge transfer coefficient (α_c) of that reaction was calculated as 0.37 ± 0.02 and 0.52 ± 0.06 on ITO and

Table 1. Elements of the EEC best fitted with the experimental data.

Electrode	Solution resistance R_s/Ω	Charge transfer resistance R_{CT}/Ω	Constant phase element Q Y_0/Mho	n	Warburg Coefficient Z_w Y_0/Mho	Fitting quality χ^2
ITO	11.1	603.7	1.79×10^{-5}	0.95	0.0333	1.4797
Pt	14.4	378.7	1.99×10^{-6}	0.91	0.0024	0.3052
PtNCFs/ITO	12.3	18.4	1.93×10^{-4}	0.86	0.0479	0.0112

Table 2. E_p^c , E_p^a , ΔE_p and $E_{p/2}^c$ of the CVs of 7.6 mg/mL $[\text{Pu}^{(IV)}(\text{SO}_4)_4 \cdot (\text{H}_2\text{O})_4]^{4-}$ in 1 M H_2SO_4 on [A] ITO and [B] PtNCFs/ITO at $\nu = 0.025, 0.050, 0.075, 0.100, 0.150, 0.200, 0.250$ and 0.300 V s^{-1} .

Electrode $\nu/\text{V s}^{-1}$	PtNCFs/ITO						ITO			
	$j_p^c/\text{mA cm}^{-2}$	E_p^c/V	E_p^a/V	$\Delta E_p/\text{V}$	$E_{p/2}^c/\text{V}$	$j_p^c/\text{mA cm}^{-2}$	E_p^c/V	E_p^a/V	$\Delta E_p/\text{V}$	$E_{p/2}^c/\text{V}$
0.025	-1.12	0.523	0.657	0.134	0.600	-0.93	0.320	0.846	0.526	0.442
0.050	-1.46	0.511	0.668	0.157	0.594	-1.09	0.295	0.882	0.587	0.415
0.075	-1.73	0.504	0.675	0.171	0.592	-1.26	0.280	0.905	0.625	0.401
0.100	-1.96	0.499	0.683	0.184	0.590	-1.43	0.266	0.919	0.653	0.394
0.150	-2.24	0.487	0.693	0.206	0.583	-1.69	0.248	0.941	0.693	0.376
0.200	-2.54	0.479	0.697	0.218	0.579	-1.91	0.232	0.958	0.726	0.365
0.250	-2.74	0.470	0.706	0.236	0.576	-2.10	0.219	0.971	0.752	0.357
0.300	-2.90	0.464	0.712	0.248	0.571	-2.33	0.209	0.981	0.772	0.351

PtNCFs/ITO, respectively, through Eq. 6 (Considering $n = 1$ for Pu(IV)/Pu(III) redox reaction):

$$n\alpha_c = \frac{0.04768}{|E_p^c - E_p^a|} \quad (6)$$

It explains the reason behind the improvement of the shape of the CVs on PtNCFs/ITO compared to ITO for the same electron-transfer reaction. The standard heterogeneous electron transfer rate constant (k_0) of this reaction on ITO and PtNCFs/ITO was calculated as 3.73×10^{-5} and $1.14 \times 10^{-3} \text{ cm s}^{-1}$ on ITO and PtNCFs/ITO, respectively from the slope of the dimensionless current (Ψ) versus $\left[\frac{n\pi F D \nu}{RT}\right]^{-\frac{1}{2}}$ as shown in Eq. 7:

$$\Psi = \frac{k_0}{\left[\frac{n\pi F D \nu}{RT}\right]^{\frac{1}{2}}} \quad (7)$$

where, D is the diffusion coefficient of Pu(IV) in 1 M H_2SO_4 (here $D = 5.0 \times 10^{-6} \text{ cm}^2 \text{ s}^{-1}$) [41] and Ψ can be calculated from the experimentally observed ΔE_p by using an empirical formula (Eq. 8) derived by Guin et al. [42]:

$$\frac{1}{\Psi} = -2.11 + (34.67 * \Delta E_p) - (19.78 * \Delta E_p^2) + (595.07 * \Delta E_p^3) \quad (8)$$

Figure 6[C] shows the cathodic and anodic square wave voltammograms (SWV) of Pu(IV)/Pu(III) redox couple in 1 M H_2SO_4 on ITO and PtNCFs/ITO electrodes. On PtNCFs/ITO electrode, the anodic peak was appeared at 0.627 V with a peak current density of 1.44 mA cm^{-2} ,

whereas on ITO electrode, the same anodic peak was appeared at 0.927 V with peak current density of $9.85 \mu\text{A cm}^{-2}$. Similarly, on PtNCFs/ITO electrode, the cathodic peak was appeared at 0.595 V with peak current density of -1.09 mA cm^{-2} , whereas on ITO electrode, the same cathodic peak was appeared at 0.28 V with peak current density of $-216.5 \mu\text{A cm}^{-2}$. Therefore, the significant increase in k_0 , decrease in R_{CT} , increase in α_c , increase in both anodic and cathodic SWV peak currents with significant decrease in the corresponding overpotentials of the Pu(IV)/Pu(III) electron transfer reaction on PtNCFs/ITO compared to ITO cumulatively showed the electrocatalytic action of PtNCFs in the electrochemistry of Pu(IV)/Pu(III) in 1 M H_2SO_4 . This study can provide some useful information about the electrochemistry of Pu(IV)/Pu(III) in 1 M H_2SO_4 among the studied electrodes modified with metal nanoparticles (as shown in Table S2 in the Supporting Information File).

4 Conclusion

The above mentioned results present a strategy of the development of cauliflower structures of Pt on ITO electrode through a multistep-coupled-oxido-reductive potentiostatic pulse sequence in an aqueous solution of platinum with a complexing electrolyte like HCl. The initial seeding of Pt-nuclei on ITO, followed by simultaneous oxidative leaching of sub-critical Pt-nuclei and surface oxidation of super-critical Pt-nuclei and then followed by reduction of surface oxides of Pt could produce in-situ fresh active sites for next nucleation event. That is how the cauliflower structures were developed over 1000 complete cycles of the above-mentioned pulse sequence. The structure of Pt helped to catalyse the

heterogeneous electron transfer of Pu(IV)/Pu(III) in dilute sulphuric acid solution compared to bare Pt and ITO electrodes. The overall studies showed that the structure and nature of the modified electrode are the key-parameters for an electrochemically quasi-reversible electron transfer reaction. Although this study is limited to the development of the template-free electrosynthesis strategy to produce PtNCFs and its influence to electron transfer reaction of Pu(IV)/Pu(III) in H₂SO₄; it keeps promise to further utilization and improvements for spectroelectrochemical determination of Pu in nuclear fuels.

Acknowledgements

Authors wish to acknowledge Dr. K. Krishnan for providing the Plutonium standard; Dr. Abhijit Ghosh and Dr. Rohan Phatak for the FE-SEM imaging and XRD analysis, respectively; Dr. S. Kannan, Dr. (Mrs) Renu Agarwal and Dr. Satyajeet Chaudhury for their kind interest and extended support in this research work.

References

- [1] S. K. Guin, K. Parvathi, A. S. Ambollikar, J. S. Pillai, D. K. Maity, S. Kannan, S. K. Aggarwal, *Electrochim. Acta* **2015**, *154*, 413–420.
- [2] C. Xie, Z. Niu, D. Kim, M. Li, P. Yang, *Chem. Rev.* **2020**, *120*, 1184–1249.
- [3] N. Narayan, A. Meiyazhagan, R. Vajtai, *Materials* **2019**, *12*, 3602.
- [4] B. Garlyyev, J. Fichtner, O. Piqué, O. Schneider, A. S. Bandarenka, F. Calle-Vallejo, *Chem. Sci.* **2019**, *10*, 8060–8075.
- [5] S. K. Guin, S. K. Aggarwal, *RSC Adv.* **2014**, *4*, 55349–55353.
- [6] S. K. Guin, J. S. Pillai, A. S. Ambollikar, A. Saha, S. K. Aggarwal, *RSC Adv.* **2013**, *3*, 17977–17988.
- [7] S. K. Guin, H. S. Sharma, S. K. Aggarwal, *Electrochim. Acta* **2010**, *55*, 1245–1257.
- [8] S. K. Guin, P. Knittel, S. Daboss, A. Breusow, C. Kranz, *Chem. Asian J.* **2017**, *12*, 1615–1624.
- [9] S. K. Guin, R. Phatak, J. S. Pillai, A. Sarkar, S. K. Aggarwal, *RSC Adv.* **2014**, *4*, 59927–59935.
- [10] M. K. Sharma, A. S. Ambollikar, S. K. Aggarwal, *Radiochim. Acta* **2011**, *99*, 17–21.
- [11] C.-T. Hsieh, J.-M. Wei, H.-T. Hsiao, W.-Y. Chen, *Electrochim. Acta* **2012**, *64*, 177–182.
- [12] J. Liu, C. Zhong, X. Du, Y. Wu, P. Xu, J. Liu, W. Hu, *Electrochim. Acta* **2013**, *100*, 164–170.
- [13] S. Li, H. Chen, J. Liu, Y. Deng, X. Han, W. Hu, C. Zhong, *ACS Appl. Mater. Interfaces* **2017**, *9*, 27765–27772.
- [14] S. J. Tauster, S. C. Fung, R. T. K. Baker, J. A. Horsley, *Science* **1981**, *211*, 1121–1125.
- [15] T. Daio, A. Staykov, L. Guo, J. Liu, M. Tanaka, S. Matthew Lyth, K. Sasaki, *Sci. Rep.* **2015**, *5*, 13126.
- [16] H. S. Sharma, N. B. Khedekar, S. G. Marathe, H. C. Jain, *Nucl. Technol.* **1990**, *89*, 399–405.
- [17] W. D. Shults, *Talanta* **1963**, *10*, 833–849.
- [18] P. R. Nair, K. V. Lohithakshan, M. Xavier, S. G. Marathe, H. C. Jain, *J. Radioanal. Nucl. Chem.* **1988**, *122*, 19–26.
- [19] S.-Y. Kim, T. Asakura, Y. Morita, *J. Radioanal. Nucl. Chem.* **2013**, *295*, 937–942.
- [20] A. M. Lines, S. R. Adami, A. J. Casella, S. I. Sinkov, G. J. Lumetta, S. A. Bryan, *Electroanalysis* **2017**, *29*, 2744–2751.
- [21] R. Gupta, J. S. Gamare, *J. Electrochem. Soc.* **2018**, *165*, H277–H283.
- [22] R. Agarwal, M. K. Sharma, *Electrochim. Acta* **2017**, *224*, 496–502.
- [23] R. Agarwal, M. K. Sharma, K. Jayachandran, J. S. Gamare, D. M. Noronha, K. V. Lohithakshan, *Anal. Chem.* **2018**, *90*, 10187–10195.
- [24] R. Gupta, S. K. Guin, S. K. Aggarwal, *RSC Adv.* **2012**, *2*, 1810–1819.
- [25] R. Gupta, J. Gamare, M. K. Sharma, J. V. Kamat, *Electrochim. Acta* **2017**, *233*, 292–293.
- [26] S. K. Guin, A. S. Ambollikar, J. V. Kamat, *RSC Adv.* **2015**, *5*, 59437–59446.
- [27] O. Ginstrop, *Acta Chem. Scand.* **1972**, *26*, 1527–1541.
- [28] D. Stoychev, A. Papoutsis, A. Kelaidopoulou, G. Kokkini-dis, A. Milchev, *Mater. Chem. Phys.* **2001**, *72*, 360–365.
- [29] G. Lu, G. Zangari, *J. Phys. Chem. B* **2005**, *109*, 7998–8007.
- [30] Z. Zhang, J. H. Lopes, S. Ye, J. T. Gostick, J. E. Barralet, G. Merle, *J. Electrochem. Soc.* **2016**, *163*, D615–D621.
- [31] Z. Liu, C. Ma, J. Liu, X. Chen, Z. Song, W. Hu, C. Zhong, *ChemElectroChem* **2017**, *4*, 66–74.
- [32] N. Hodnik, C. Baldizzone, G. Polymeros, S. Geiger, J.-P. Grote, S. Cherevko, A. Mingers, A. Zeradjanin, K. J. J. Mayrhofer, *Nat. Commun.* **2016**, *7*, 13164.
- [33] Y. Sugawara, T. Okayasu, A. P. Yadav, A. Nishikata, T. Tsuru, *J. Electrochem. Soc.* **2012**, *159*, F779–F786.
- [34] D. Gilroy, B. E. Conway, *Can. J. Chem.* **1968**, *46*, 875–890.
- [35] P. P. Lopes, D. Tripkovic, P. F. B. D. Martins, D. Strmcnik, E. A. Ticianelli, V. R. Stamenkovic, N. M. Markovic, *J. Electroanal. Chem.* **2018**, *819*, 123–129.
- [36] S. Geiger, S. Cherevko, K. J. J. Mayrhofer, *Electrochim. Acta* **2015**, *179*, 24–31.
- [37] B. R. Shrestha, E. Tada, A. Nishikata, *Electrochim. Acta* **2014**, *143*, 161–167.
- [38] B. Scharifker, G. Hills, *Electrochim. Acta* **1983**, *28*, 879–889.
- [39] L. V. Lipis, B. G. Pozharskii, V. V. Fomin, *J. Struct. Chem.* **1960**, *1*, 390–396.
- [40] A. J. Bard, L. R. Faulkner, *Electrochemical Methods: Fundamentals and Applications*, Wiley, **2006**.
- [41] D. G. Peters, W. D. Shults, *J. Electroanal. Chem.* **1964**, *8*, 200–229.
- [42] S. K. Guin, A. S. Ambollikar, J. P. Guin, S. Neogy, *Sens. Actuators B* **2018**, *272*, 559–573.

Received: March 16, 2020

Accepted: April 24, 2020

Published online on May 20, 2020